$Eu_2SrCo_{1.5}Mn_{0.5}O_7$ a new promising compound as cathode in intermediate temperature solid oxide fuel cells

Khalid Boulahya,[*[a]] Manar Hassan,[[a]] Daniel Muñoz Gil,[[a]] Julio Romero,[[b]] AdriánGómez Herrero,[[c]] Susana García Martin,[[a]] Ulises Amador[[d]]

[a] Departamento de Química Inorgánica, Facultad Ciencias Químicas, Univ. Complutense, E-28040 Madrid, Spain.

[b] CAI Técnicas Físicas, Facultad de Ciencias Físicas, Univ Complutense de Madrid, E-28040 Madrid, Spain.

[c]Centro Nacional de Microscopía Electrónica, Universidad Complutense, E-28040 Madrid, Spain

[d]Departamento de Química, Facultad de Farmacia, Universidad CEU San Pablo, Urb. Montepríncipe, Boadilla del Monte, E-28668, Madrid, Spain.

Abstract

A new oxide of the Ruddlesden–Popper series has been isolated and structurally characterized in the Eu-Sr-Co-Mn-O system. X-ray diffraction and electron microscopy show that polycrystalline $Eu_2SrCo_{1.5}Mn_{0.5}O_7$ constitutes the n=2 member of a homologous series, the essential feature of which is the existence of two connected Co/Mn octahedral layers, separated by Eu atoms. Electrochemical study shows that, the area-specific resistance of this compound is 0.15Ω cm^2 at 700 ºC in air, a performance which is comparable to that of the best state-of-the-art materials used as cathode in intermediate temperature solid oxide fuel cells. Below 150 K the title material presents two different magnetic phenomena. The first one corresponds to the formation of ferromagnetic nanoclusters (T_C~121 K) within an ordered Co^{2+}/Mn^{4+} atomic configuration, whereas at lower temperature (~21 K)a spin glass state occurs with no conduction electrons.

Introduction

Manganites and cobaltites are among the most relevant perovskite-related oxides under study due to their enormous ability to adopt different structures and properties. In this sense, magnetic, electrical and catalytic properties make them promising materials for different applications. For instance, in addition to the interesting electrical properties of the system$La_{1-x}Sr_xCoO_{3-y}$[1], giant magnetoresistance has been found in $La_{1-x}(Ba,Sr,Ca)_xCoO_{3-y}$[2] whereas thermoelectric power properties have been reported for $Ca_3Co_4O_9$[3]. The richness of the physical properties of cobaltites is related to the ability of Co ions to adopt, not only several oxidation states, but also different spin states.

Precise knowledge of the relationships between structure and properties is crucial for the design of efficient materials. In the search for these relationships, the great flexibility of perovskite-type oxides $ABO_3$to accommodate the insertion of AO rock salt layers is extremely useful. The ability of the cubic perovskite (ABO_3) and the rock salt (AO) structures to intergrowth in an ordered way along [001] stacking direction leads to two-dimensional layered perovskites that have been widely studied from the structural point of view [4-8].

The magnetic and electric properties in addition to the excellent chemical and thermal stability of cobalt perovskite related oxides that belong to the Ruddlesden–Popper (R–P) series [7, 8]with the general formula $A_{n+1}B_nO_{3n+1}((ABO_3)_nAO)$ (A=Rare and/or alkaline earth elements and B= transition metal), in which the multiple perovskite layers that are n octahedra thick alternate with single AO rock salt layers, make them very attractive materials.

The magnetic properties of some $A_{n+1}B_nO_{3n+1}$ members have been subject of intensive studies. For instance, substitution of Fe by Co in the $PrSr_3Fe_3O_{10}$ (n=3) introduces

ferromagnetic interactions that dramatically increase the conductivity at low temperature. A random Co distribution results in a local magnetic frustration and possibly also in the formation of nanoscopic magnetic clusters[9].On the other hand, other R-P-like materials such as $Sr_3(Fe_{1-x}Co_x)_2O_7$ (n=2) presents an interesting magnetic phase diagram where magnetic interactions evolve from anti-ferromagnetic (AFM) via spin glass (SG) to ferromagnetic (FM) with increasing Co content[10].

The discovery of high oxide ion conductivity in $A_{n+1}B_nO_{3n+1}$ oxides has increased the search of new members of the Ruddlesden–Popper homologous series as electrodes for Intermediate Temperature Solid Oxide Fuel Cells (IT-SOFCs)[11-16]. Among the R–P series, the interest has been mainly focused on the n=1 intergrowth oxides, where one-octahedron-thick layers alternate with single AO rock salt layers along packing axis[11, 15, 16] though there are some articles reporting the properties of n=2 and 3 members.[12-14] All of these R-P series present perovskite-like blocks where electronic conduction may occurs when built of MO_6 octahedra where M-cations can present multiple non-localised oxidation states and AO rock salt layers with interstitial oxygen ions and/or non-occupied sites allowing the formation of anionic Frenkel defects both resulting in ionic conduction.

In general, Co-R-P oxides exhibit high catalytic activity for oxygen reduction and high electronic conductivity but relatively high thermal expansion coefficients (TEC), like the Co-perovskites. Substitution of Co by Cu or Fe decreases TEC, however, decreases the electronic conductivity and increases the area specific resistance (ASR)[17-20].

In this study, $Eu_2SrCo_{1.5}Mn_{0.5}O_7$a new member n=2 of Ruddlesden–Popper (R–P) series $(Eu,Sr)_{n+1}(Co,Mn)_nO_{3n+1}$has been prepared. A detailed characterisation by means of X-ray diffraction and electron microscopy has been performed to elucidate the compound´s

structure. Besides, its magnetic and electrochemical properties as cathode for IT-SOFCs have been explored.

Experimental

Polycrystalline $Eu_2SrCo_{1.5}Mn_{0.5}O_7$ was synthesized by heating stoichiometric amounts of $SrCO_3$ (*Aldrich 99.98%*), Co_3O_4 (*Aldrich 99.9%*) and Eu_2O_3 (*Aldrich 99+%*)/ MnO_2 (*Aldrich 99+%*) in air at 1200ºC for 7 days, and then quenched to room temperature.

Sample purity was determined by powder X-ray diffraction (PXRD) (these data were also used for the structure characterization) on a Bruker D8 high-resolution diffractometer equipped with a LynxEye® fast detector using monochromatic $CuK_{\alpha 1}$ (λ = 1.5406 Å) radiation obtained with a germanium primary monochromator. The angular range, step size and counting times were selected so as to ensure the required data quality and resolution for structural refinement. Diffraction data were analyzed using the Fullprof software[21]; peak shape was described by a pseudo-Voigt function, and the background level was fitted with linear interpolation.

The sample was characterized by High Resolution Transmission Electron Microscopy (HRTEM) by using a JEOLJEM-3000F electron microscope operated at 300kV.Scanning Transmission Electron Microscopy (STEM) was performed on a JEOL JEM-ARM200cF microscope (Cold Field Emission Gun) operated at 200 kV. The microscope is provided with a spherical aberration corrector in the electron probe (probe current ~ 20pA for a probe size ~0.8 Å, convergence semi-angle~ 25 mrad, collection semi-angles of 90-170 mrad for High Angle Annular Dark Field (HAADF) STEM imaging and 11-22 mrad for Annular Bright Field (ABF) STEM imaging). Local composition was analysed by energy-dispersive X-ray

spectroscopy (EDS) with an INCA Oxford analyser system attached to above mentioned electron microscopes.

The average oxidation state of 3d-ions (Co and Mn) and oxygen content (assuming charge neutrality) of samples were determined by titration as described in ref. [22].

Magnetic measurements were performed using a superconducting quantum interference device magnetometer (Quantum Design, model MPMS-XL).The dc magnetic susceptibility (χ) was obtained in the temperature range 2-300 K at 100 mT, after cooling the sample from room temperature to 2 K in zero field and also after cooling in the measuring field. These are the zero field cooling (ZFC) and field cooling (FC) protocols, respectively. The real and imaginary components of ac magnetic susceptibility (χ'_{ac} and χ''_{ac}, respectively) were obtained in the temperature range 2-200 K applying an oscillating magnetic field with drive amplitude of 0.35 mT at different frequencies. The magnetic field dependence of dc magnetization was measured at different temperatures in magnetic fields strengths up to 5 T. The diamagnetic contribution from each ion present in the materials was considered to analyse the experimental data[23].

The electrochemical performance of $SrEu_2Co_{1.5}Mn_{0.5}O_7$ as cathode in IT-SOFCs has been evaluated by determination of area-specific resistances (ASRs) at different temperatures in air. The ASR (resistance associated to the total electrochemical processes at the electrodes) has been determined by impedance spectroscopy (IS) on symmetrical two-electrode configuration cells. Electrolyte pellets of about 8.6 mm diameter and around 1.10 mm thickness of commercial $Ce_{0.9}Gd_{0.1}O_{2-\delta}$ (CGO) powder (Fuel Cells Materials) were prepared by pressing the powder at 250 MPa and sintering in air at 1400 ºC for 12 hours (heating/cooling rate of 2.5 ºC min^{-1}). Thin layers of slurries prepared by

$SrEu_2Co_{1.5}Mn_{0.5}O_7$:CGO composites (70:30 wt %) using Decoflux™ as a binder were deposited onto both surfaces of the electrolyte and then fired at 900 ºC for 3h in air (heating/cooling rate of 2.5 ºC min^{-1}). Silver paste and silver mesh were used as current collectors. The IS measurements cells were carried out in air on heating and cooling cycles between 500 ºC and 700 ºC using a frequency response analyser (Solartron 1255 + dielectric interface 1296) in the frequency range 0.1 Hz to 1 MHz with an excitation voltage of 50 mV. The impedance spectra were fitted to equivalent circuits using the Zview software.[24] The ASR values have been determined from the resistance obtained by extracting the electrolyte resistance (taking into the account the high and low-frequency x-axis intercepts) corrected for the electrode area and divided by 2, as it is common in symmetrical cells.[25, 26]

Chemical compatibility of the $SrEu_2Co_{1.5}Mn_{0.5}O_7$ compound with the CGO was proven prior to the electrochemical studies: $SrEu_2Co_{1.5}Mn_{0.5}O_7$:CGO composite (70:30 wt %) was heated at 900 ºC for 12 hours and further analysed by PXRD. The microstructure of the electrochemical cells was evaluated by scanning electron microscopy (SEM) before and after the impedance measurements using a FEI XL30 scanning electron microscope. Thermogravimetric analysis (TGA) was carried out in air to evaluate oxygen stoichiometry stability of the $SrEu_2Co_{1.5}Mn_{0.5}O_7$ from 25 ºC to 900 ºC.

Results and Discussion

Structural Characterisation. The sample of nominal composition $Eu_2SrCo_{1.5}Mn_{0.5}O_7$ was confirmed to be single phase by PXRD since the whole pattern can be indexed on the basis of a tetragonal unit cell with lattice parameter a=5.4011(2) Å and c =19.6054(8) Å. The reflection conditions ((*0kl) k+l=2n, (0k0) k=2n and (00l) l=2n)*) allow determining the

possible Space Groups (S.G.) to be $P4_2nm$ (#102), P-4n2(#118) and $P4_2/mnm$ (#136).In this connection, the structure of $Eu_2SrFe_2O_7$[4, 5, 27]oxide was previously described in the$P4_2/mnm$ S.G.

Selected Area Electron Diffraction (SAED) patterns and HRTEM micrographs along several zone axes were taken on crystals of $Eu_2SrCo_{1.5}Mn_{0.5}O_7$ in order to fully reconstruct the reciprocal and real space. The most relevant zone axis, corresponding to [1-10] and [010] are shown in Figures 1 and 2, respectively. All reflections can be indexed in the primitive tetragonal lattice determined by PXRD (a=5.4Å and c=19.6 Å); moreover, the observed reflection conditions confirm the symmetries deduced from that technique. The HRTEM micrograph taken along [1-10] (Figure 1) shows an apparently well-ordered material with d-spacing of 1.9 Å and 9.8 Å, corresponding to d_{220} and d_{002}. The contrast observed in this image corresponds to bright dots alternating with a brightest one, which can be associated to the Sr/Eu atoms alternating with Co/Mn ones along [001] as shown in the model depicted at the inset of Figure 1. Such contrast variation is characteristic of n=2 member of Ruddlesden–Popper series as observed in references.[4, 5] No evidence of microdomains, neither extra spots nor diffuse scattering that could be a sign of additional order were observed in the corresponding diffraction patterns or Fourier transforms of the HRTEM images.

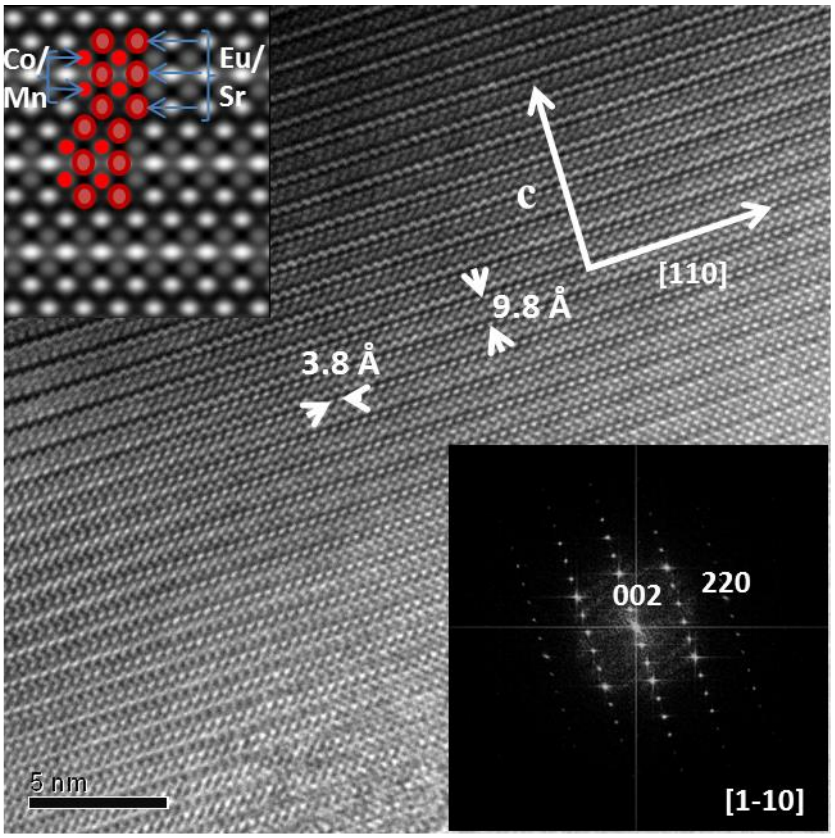

Figure 1. HRTEM image of $Eu_2SrCo_{1.5}Mn_{0.5}O_7$ along the [1-10] zone axis. Insets shows; corresponding optical Fourier transform (FT) and Image magnification where metal atoms are superimposed.

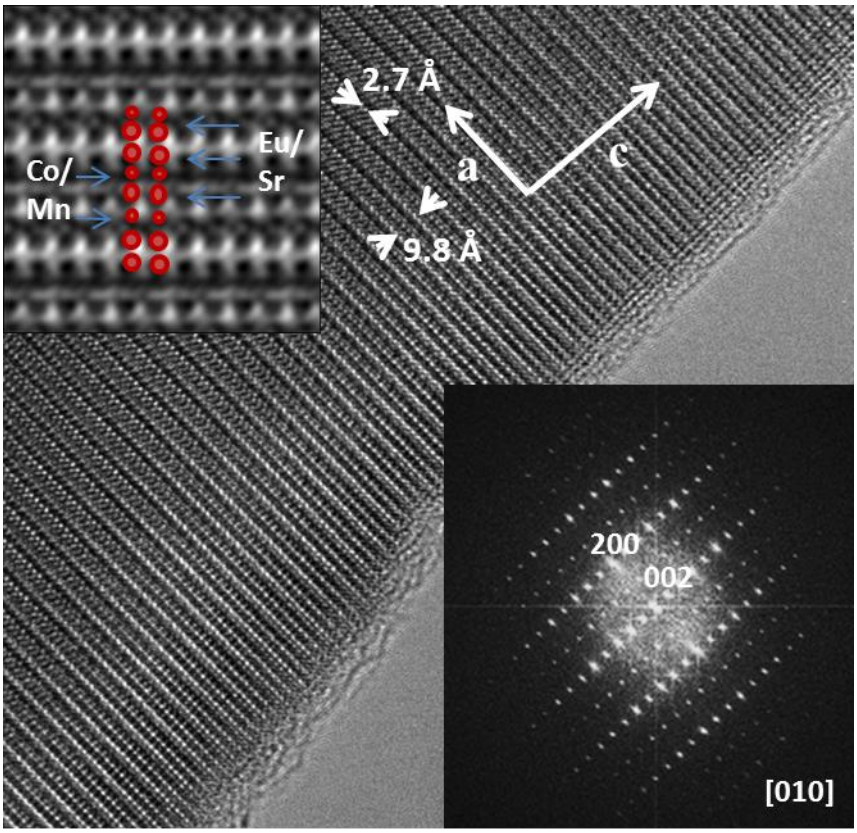

Figure 2. HRTEM image of $Eu_2SrCo_{1.5}Mn_{0.5}O_7$ along the [010] zone axis. Insets shows; corresponding optical Fourier transform (FT) and an enlarged image where metal atoms have been superimposed.

The HRTEM micrograph taken along the [010] direction (Figure 2), reveals an apparently well-ordered material with d-spacing of 2.7Å and 9.8 Å, corresponding to d_{200} and d_{002}. Fourier transform was performed on the micrograph, looking for the presence of different domains that could evidence the existence of additional ordering or intergrowth of different members of Ruddlesden–Popper series. Since no extra spots nor diffuse scattering are observed any kind of additional order can be discarded.

To elucidate in detail the structure of $Eu_2SrCo_{1.5}Mn_{0.5}O_7$compound a HAADF and ABF STEM study with atomic resolution has been performed. HAADF-STEM imaging provides

images of the crystal structure which in most cases are directly interpretable: the contrast is roughly proportional to the average Z^n (n ~ 1.7) of the atomic columns being imaged[28-31], however, the oxygen (and other light elements) columns are barely visible in the presence of heavier atoms. A HAADF-STEM image along [010] is shown in Figure 3a, the atomically resolved columns corresponding to Eu, Sr and Co/Mn, are clearly observed arranged in an ordered intergrowth along the c-axis. The brightest dots are related to the heaviest atoms Eu, whereas those of intermediate intensity are Sr, the less intense ones correspond to Mn/Co atoms. These structural features agree with those reported for $Eu_2SrFe_2O_7$[27].

Figure 3b shows the ABF STEM image that was recorded simultaneously. This imaging mode allows reliably revealing both light and heavy atom columns over a range of thickness and defocus values.[28, 31] In contrast to HAADF imaging, both light and heavy atom columns are imaged as dark spots.[29, 30] However, this imaging technique does not provide a direct correspondence between contrast and ~Z^2 as HAADF. In any case, the structural models obtained by both techniques nicely match. Even more, oxygen atoms are revealed as weak but clearly resolved spots. A schematic projection of the structure model of $Eu_2SrCo_{1.5}Mn_{0.5}O_7$ compound based on that of $Eu_2SrFe_2O_7$depicted in the inset of Fig. 3b helps to interpret the contrasts observed. Interestingly, the oxygen positions are sufficiently clear in the experimental image to allow revealing subtle structural details such as tilting of the corner-sharing octahedral BO_6 (B = Co, Mn). Direct visualization of octahedral tilting in perovskite oxides by ABF-STEM has been previously reported by Aso et al.[32]

A schematic representation of the structure is superimposed on Fig 3b. Interestingly, interstitial oxygen atoms are detected within rock-salt like EuO layers, which are indicated by blue arrows in the figure.

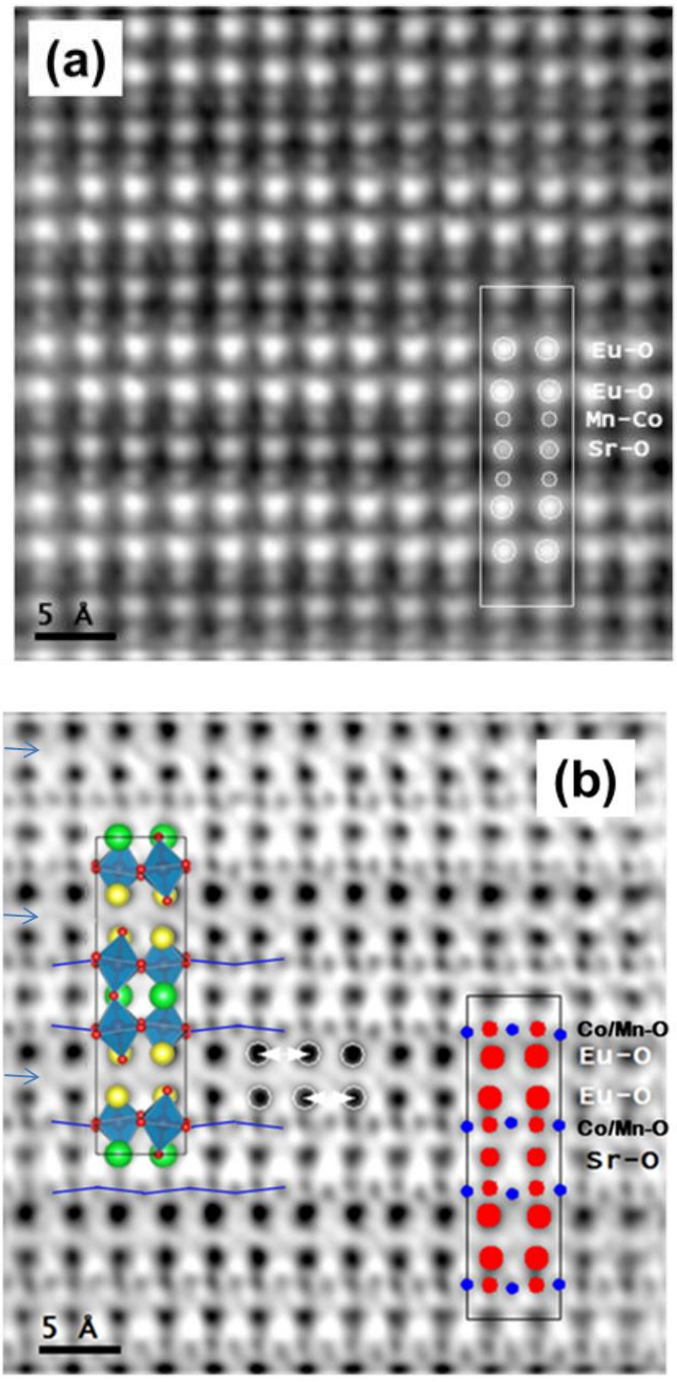

Figure 3. (a) HAADF image of along $Eu_2SrCo_{1.5}Mn_{0.5}O_7$ [0 1 0]. A schematic model for cationic position has been inserted. **(b)** Corresponding ABF image where cationic atoms are in red and oxygen are in blue. Interstitial oxygen ions are indicated by blue arrows.

Using the above results we have developed a structural model for $Eu_2SrCo_{1.5}Mn_{0.5}O_7$based on the structure of $Eu_2SrFe_2O_7$ (n=2 member of the R-P series of layered compounds) with symmetry $P4_2/mnm$[27]. PXRD data have been used to confirm the validity of this model, derived from local techniques, to describe the average structure of the title compound.

It is well established that partial ordering of Sr^{2+} and Ln^{3+} ions can occur in similar R-P oxides $Sr_{2-x}Ln_xMn_2O_7$ along the two A-cations sites; the smaller lanthanides are mainly located in the rock-salt layers whereas larger Sr^{2+} prefer the A-sites in the perovskite blocks[33]. Thus, the Eu/Sr distribution over the two crystallographically distinct A-sites was refined and complete cationic ordering was determined. Since no evidence of Co/Mn order in the B sublattice was detected, both cations were randomly distributed over the octahedral sites. The refinement was stable provided a Debye-Waller for each kind of atom was used (same for all the oxygens). Thus, it was possible to refine the positions and occupancies of all atoms (since Mn and Co are indistinguishable by XRD theirs contents were assumed as the nominal ones); given full population of all sites within the experimental error (including oxygen atoms), so no vacancies are produced in the anion sub-structure. Interestingly, chemical titration confirms this result since the average oxidation state of 3d-metals is determined to be 2.99(2); assuming electroneutrality the oxygen content is 6.99(3).

Random distribution of 3d-metals in high oxidation states is commonly associated to high electronic conduction in oxides.

Figure 4 shows the graphic results of the fitting of the experimental X-ray diffraction pattern and the difference between observed and calculated data.

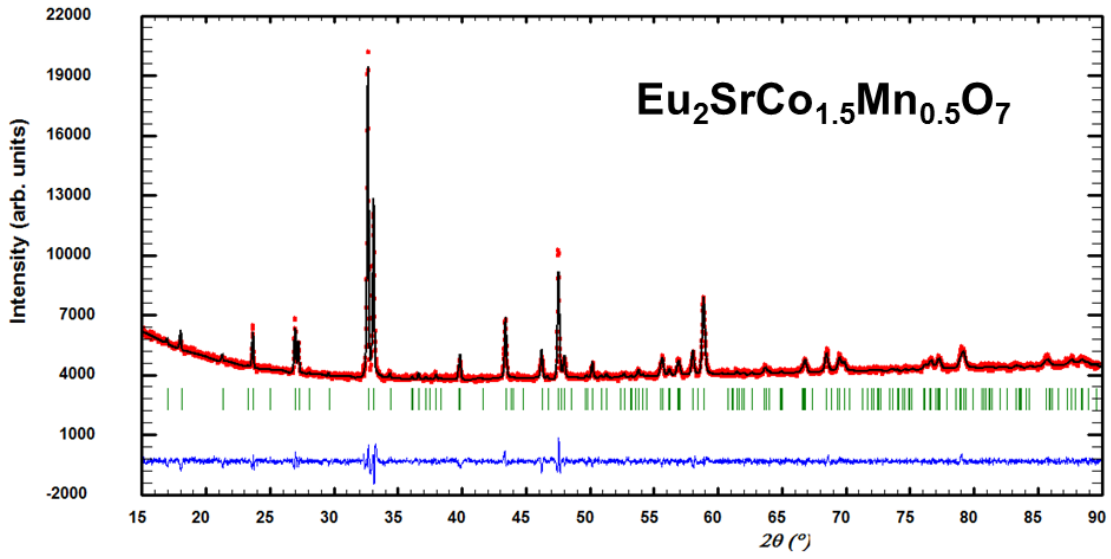

Figure 4. Experimental (red points), calculated (solid black line) and their difference (blue line at bottom) X-ray diffraction patterns for $Eu_2SrCo_{1.5}Mn_{0.5}O_7$. The vertical bars (green) indicate the positions of the Bragg peaks.

The final refined structural parameters are collected in Table 1, whereas Table 2 shows some selected interatomic distances. The structure refinement confirms that it is isostructural with $Eu_2SrFe_2O_7$ [27] in agreement with the HRTEM results. In Figure 5 a schematic representation of the structure is depicted.

Interestingly, in the cubic-perovskite-like blocks (i.e. corner-sharing octahedra), tilting of the BO_6polyhedra occurs with a Glazer[34]scheme ($a^-a^0c^0$) (block at the bottom of the unit cell) and ($a^0a^-c^0$) /block at the middle of the cell. That is, in every two-layer blocks out-of-phase tilt occurs along one of the pseudo-perovskite axis, being the direction of tilting rotated by 90º from one block to the adjacent ones. Along the four-fold axis no tilt is produced. Similarly in other layered perovskites such as the 12R-type hexagonal $Sr_3NdNb_3O_{12}$the octahedra of the three-layer blocks are tilted along the Cartesian *x*, *y* and *z* axes of the pseudocubicsubcell according to the ($a^-a^-a^-$) tilt system[35].

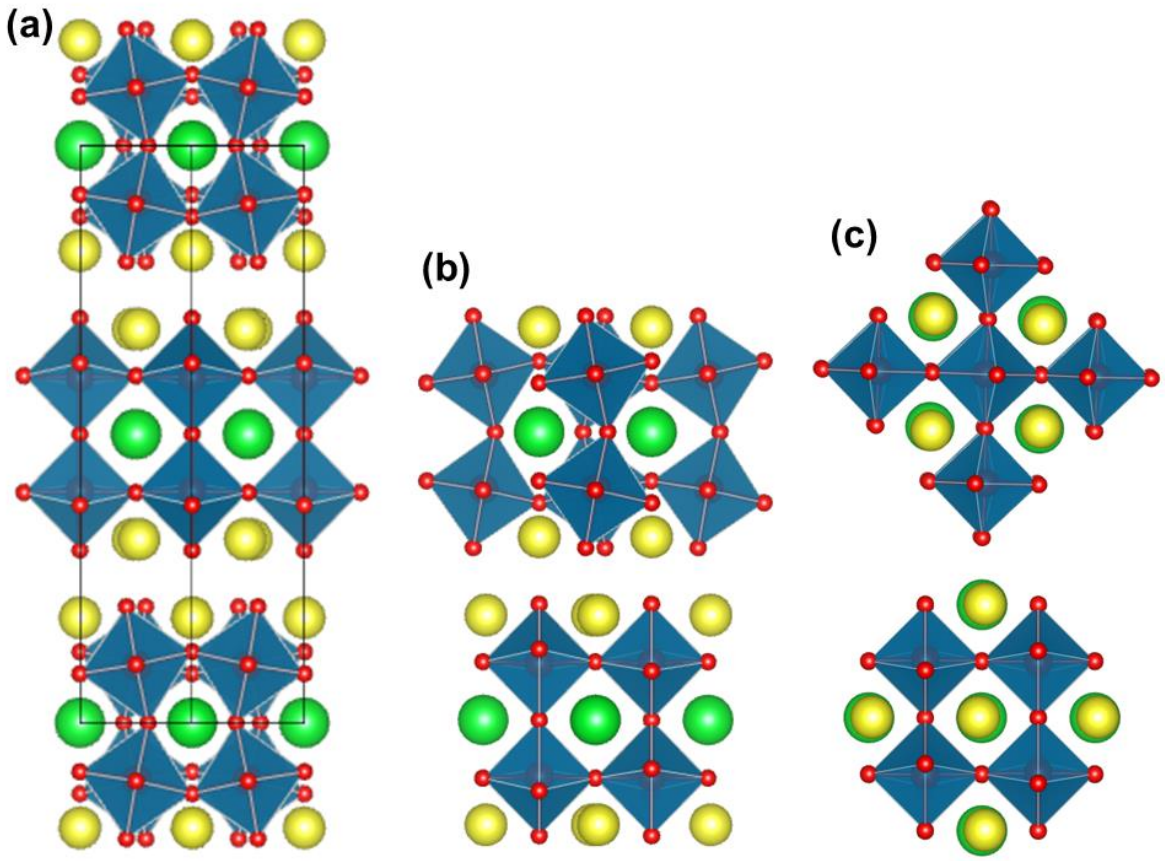

Figure 5. (a) Schematic representation along the [110] direction of the structure of $Eu_2SrCo_{1.5}Mn_{0.5}O_7$, **(b)** view along [1-10] of the perovskite blocks and **(c)** view along the c-axis of those blocks. Co and Mn are located at the center of blue octahedra of oxygen atoms (small red balls); green balls represent Sr ions whereas yellow ones correspond to Eu.

Unfortunately, other structural features strongly related with electrical properties (in particular with ionic conduction) such as the existence of anion vacancies and interstitial oxygen ions, cannot be fully stablished using XRD. On the contrary, a close inspection of the ABF-STEM image seems to indicate the possible presence of interstitial oxygen atoms located in between two Eu-O planes. A diffuse contrast at the centre of four E-O columns,

indicated by blue arrows, is observed in the ABF-STEM image along the [0 1 0] zone axis (Fig. 3b), which might be related with the location of some oxygen atoms.

Table1: Structural parameters for $Eu_2SrCo_{1.5}Mn_{0.5}O_7$ obtained from XRD data.

a (Å)	5.4011(2)		
c (Å)	19.6054(9)		
Eu position 8j		**O(1) position 8h**	
x	0.2365(7)	**z**	0.399(2)
z	0.1820(6)	**Occ.**	1.02(4)
Occ.	1.00	**U*100 (Å^2)**	0.61(8)
U*100 (Å^2)	0.56(5)	**O(2) position 8j**	
Sr position 4f		**x**	0.294(3)
x	0.2487(6)	**z**	0.299(1)
Occ.	1.00	**Occ.**	1.00(3)
U*100 (Å^2)	0.58(6)	**U*100 (Å^2)**	0.61(8)
Co/Mn position 8j		**O(3) position 4e**	
x	0.2467(5)	**z**	0.085(4)
z	0.4011(7)	**Occ.**	0.99(2)
Occ. Co/Mn	0.75/0.25	**U*100 (Å^2)**	0.61(8)
U*100 (Å^2)	0.54(4)	**O(4) position 4e**	
		z	0.377(3)
		Occ.	1.02(3)
		U*100 (Å^2)	0.61(8)
		O(5) position 4g	
		x	0.304(4)
		Occ.	1.01(2)
		U*100 (Å^2)	0.61(8)

Space Group $P4_2/mnm$ (#136): 4e (0 0 z), 4f (x x 0), 4g (x –x 0), 8h (0 ½ z), 8j (x x z)
χ^2= 2.59, R_{wp}= 2.44%, R_{exp}= 1.51%, R_B= 4.91%

Table 2: Selected structural information for $Eu_2SrCo_{1.5}Mn_{0.5}O_7$ obtained from XRD data. Angles are given in degrees and distances in Å, distortion Δ of the BO_npolyhedra is given as $\Delta = 1/n\ \Sigma_{j=1,n}\ \{(d_n - \langle d(B\text{-}O)\rangle) / \langle d(B\text{-}O)\rangle\}^2$ and $t = \langle r(A)\rangle + r(O) / \sqrt{2}\ \langle r(B)\rangle + r(O)$.

Eu	O(1)	2.487(8) x 2
	O(2)	2.335(7)
	O(2)	2.429(8) x 2
	O(3)	2.624(7)
	O(4)	2.322(7)
average Eu-O		2.444(7)
distortion EuO_7 ×10^{-4}		15.067
Sr	O(1)	2.751(5) x 4
	O(3)	2.529(6) x 2
	O(5)	2.431(6) x 2
average Sr-O		2.615(6)
distortion SrO_8 ×10^{-4}		26.657
Co/Mn	O(1)	1.910(4) x 2
	O(2)	2.034(4)
	O(3)	1.959(6)
	O(4)	1.938(4)
	O(5)	1.975(4)
average Co/Mn-O		1.954(5)
distortion (Co/Mn)O_6 ×10^{-4}		6.746
tilt angle[a]		20.3(1)

[a] along [110] pseudocubic axis in a given two-layer perovskite block and along [-110] direction in adjacent blocks.

Physical Properties

Magnetic behaviour.

The magnetic behaviour of oxides is related to metal oxidation states, charge localization and ordering phenomena, which are also related with transport properties. Thus, magnetic measurements may help to understand the electrical properties of a given material.

Figure 6 shows the temperature dependence of the molar magnetic susceptibility,χ, for $Eu_2SrCo_{1.5}Mn_{0.5}O_7$ measured under zero-field-cooled (ZFC) and field-cooled (FC) conditions at 100 mT. Both curves reveal a paramagnetic behaviour from room temperature down to 150 K following the Curie-Weiss law $\chi=C/(T-\theta)$. The best fit of the data to this law yields C=7.241±0.009 emu K mol^{-1} Oe^{-1} and θ=25.2 ±0.2 K and no temperature-independent term must be added for it, on the contrary to what observed in other SOFC-cathode materials with high electronic conductivity[36]. Thus, Pauli paramagnetism associated to mobile electrons in the material and to a metallic-like behaviour can be discarded and then $Eu_2SrCo_{1.5}Mn_{0.5}O_7$ most likely will present a semiconductor character. Furthermore, the value of the magnetic moment calculated at room temperature for $Eu_2SrCo_{1.5}Mn_{0.5}O_7$, $\mu = \sqrt{\chi T} = 7.95\ \mu_B$, indicates the presence of magnetic moments bounded tolocalised electrons according to the Curie-Weiss behaviour of χ. However, this value of the total magnetic moment is irreconcilable with whatever cationic scenario it may be considered according to the average oxidation state of 3d-metals above mentioned, if single spin state is assumed for the octahedrally coordinated Co^{3+} cations. Therefore, in this oxide the Co^{3+} must show a mixed-spin state, which likely consists of low-spin (LS) and high-spin (HS) states being Co^{3+} ad^6 ion.[37]The coexistence of these two spin states (one of them diamagnetic) together with the random distribution of cobalt and manganese atoms over the two octahedral thick perovskite layers will play an important role in the magnetic behaviour observed at low temperature.

Upon cooling from 150 K, see Figure 6a, χ goes on rising with a noticeable increase in the slope below 135 K, and the ZFC and FC curves remain coincident down to ~100 K. Below this temperature the ZFC χ shows a tenuous hump at ~94 K, then it rises to reach a maximum

at 21 K, and finally it drops at lower temperature. On its hand, the FC χ continuously increases as the temperature is lowered and just below 21 K the rate of signal growing abruptly decreases. The first magnetic phenomenon, taking place at 135 K, is more evident in the variation of the ac magnetic susceptibility χ_{ac} with temperature, see Figure 6b. Thus, as temperature decreases from 150 K, the rising χ'_{ac} shows a slight increment of slope at ~123 K followed by a small maximum at 118 K, and a very weak absorption at 121 K takes place in χ''_{ac}. These features are independent on the measuring frequency and therefore they could indicate the onset of ferromagnetism at 121 K due to Mn^{4+}–O–Co^{2+}superexchange interaction that becomes operative at that temperature.[38] In this sense, the synthesis temperature and the quenching process allow the coexistence of Co^{2+} and Mn^{4+} (in equal molar quantities) together with Co^{3+} and Mn^{3+}.[39] Thus, according to the tenuous magnetic transition observed (T_C= 121 K) and the HRTEM results, we can assume the ferromagnetism develops within short-range ordered regions (clusters), which will be embedded in a matrix mainly formed by Co^{3+} (LS/HS) cations with a certain amount of Mn^{3+} cations randomly distributed.[40, 41]

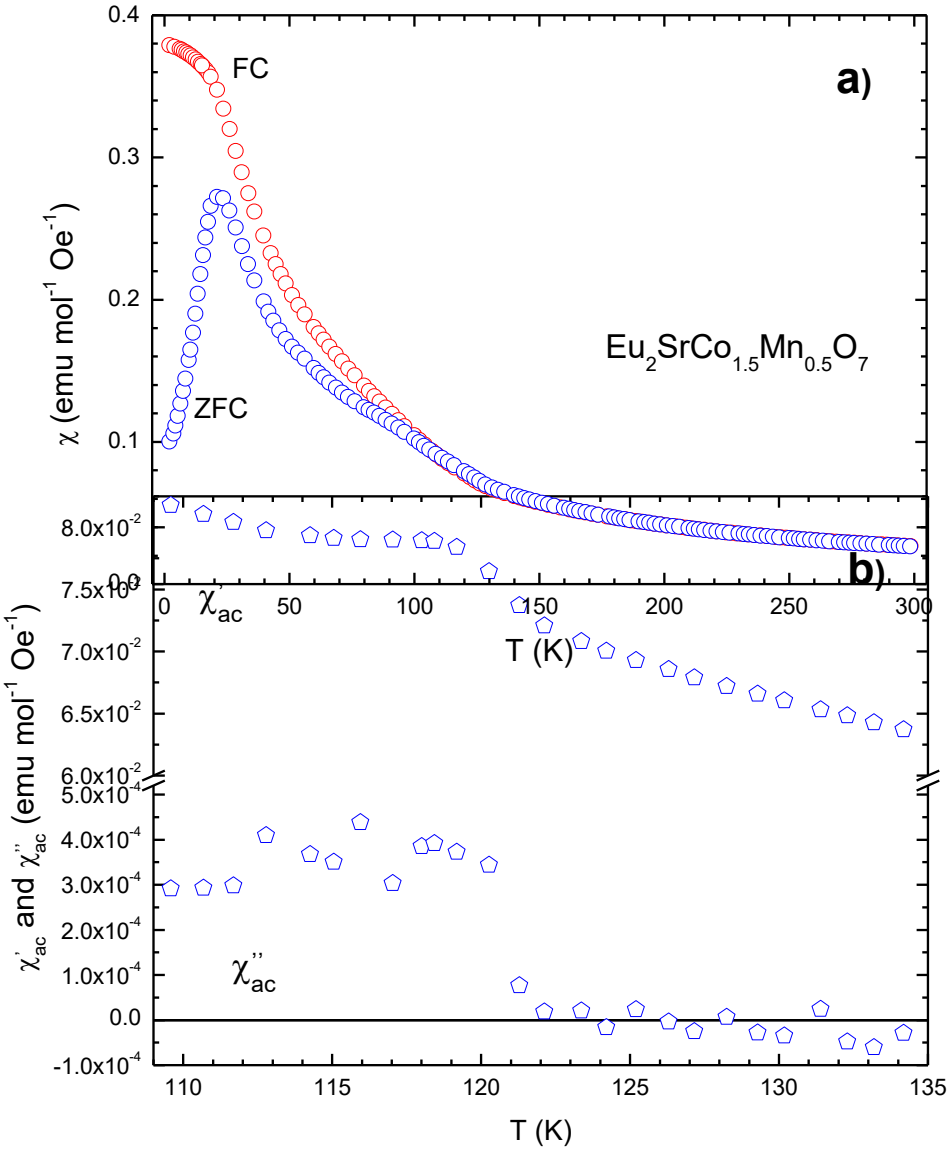
a)
FC
ZFC
$Eu_2SrCo_{1.5}Mn_{0.5}O_7$
χ (emu mol^{-1} Oe^{-1})
b)
χ'_{ac}
T (K)
χ'_{ac} and χ''_{ac} (emu mol^{-1} Oe^{-1})
χ''_{ac}
T (K)

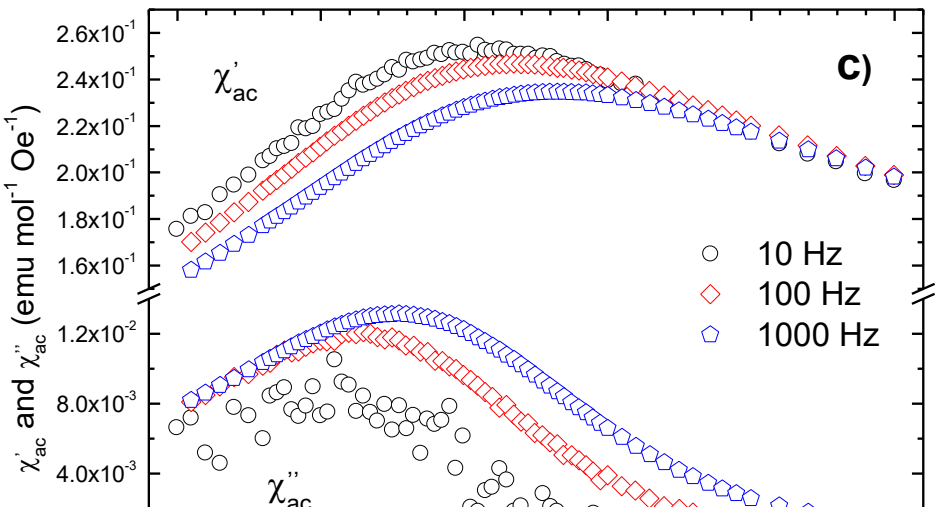
c)
χ'_{ac}
10 Hz
100 Hz
1000 Hz
χ'_{ac} and χ''_{ac} (emu mol^{-1} Oe^{-1})
χ''_{ac}

Figure 6. (a) Molar magnetic susceptibility vs. temperature curves for $Eu_2SrCo_{1.5}Mn_{0.5}O_7$ oxide as measured in an applied field of 100 mT following the zero-field cooled (ZFC) and field-cooled (FC) protocols. **(b)** Temperature dependence in the range 108-135 K of the real part (χ'_{ac}) and the imaginary part (χ''_{ac}) of the ac magnetic susceptibility measured at a driving field of 0.35 mT with 1000 Hz. **(c)** Temperature dependence in the range 15-40 K of χ'_{ac} and χ''_{ac} measured at a driving field of 0.35 mT with frequencies 10, 100 and 1000 Hz.

Finally, concerning the second magnetic anomaly taking place at 21 K, Figure 6c shows the variations of χ'_{ac} and χ''_{ac} with temperature and frequency (f). χ'_{ac} presents a broad maximum centred at a temperature (T_{max}) higher than 21 K which is shifted towards higher temperatures as frequency is increased, whereas its intensity decreases. χ''_{ac} also shows a broad maximum, centred at lower temperatures than χ'_{ac}, that is enhanced and shifted towards higher temperatures as frequency is increased. This behaviour is usual for the onset of a spin glass state and for the blocking of superparamagnetic particles, but the frequency shift value of ~0.056, calculated according to the expression $\Delta T_{max}(T_{max})^{-1}[\Delta(\log f)]^{-1}$, is indicative of a freezing process of a spin glass with no conduction electrons.[42] This spin glass ground state can occur through non-negligible interaction between the ferromagnetic clusters previously mentioned, or through the presence of magnetic frustration in the disordered Co^{3+}-rich/Mn^{3+} matrix introduced by the competition between ferromagnetic and antiferromagnetic interactions as, for example,Co^{3+}(HS)–O–Mn^{3+} and Co^{3+}(HS)–O–Co^{3+}(HS) superexchange interactions, respectively. To distinguish between intercluster interactions and the presence

of a conventional spin glass phase requires a deeper study that well exceeds the scope of this work.

Therefore, magnetic measurements suggest that at temperatures corresponding to IT-SOFC operation $Eu_2SrCo_{1.5}Mn_{0.5}O_7$ will present a semiconductor behavior according to the presence of a majority cobalt-rich disordered Co/Mn atomic configuration, with a HS Co^{3+}/LS Co^{3+}/Mn^{3+} valence state; together with short-range Co/Mn atomic ordering with a Co^{2+}/Mn^{4+} valence state.

Electrochemical performance

Chemical stability and compatibility

Prior to be used as components in IT-SOFC electrodes, the chemical stability of the title material as well as its compatibility with the electrolyte (CGO) was evaluated in simulated processing and working conditions. Since $Eu_2SrCo_{1.5}Mn_{0.5}O_7$is prepared by quenching from high temperature (1200ºC), it exists as a metastable phase at lower temperatures. Therefore, it is relevant to determine whether it evolves (decomposes) in the IT-SOFC conditions. A small amount of the material was fired at 800 ºC for several days (14 days) and slowly cooled down to room temperature. The corresponding PXRD pattern (not shown) allowed discarding any decomposition. Besides, TGA analyses (not shown) in oxidizing atmosphere (air) reveal that the material does not experience any significant oxygen loss or gain when repeatedly submitted to cycles from RT to 900ºC.

$SrEu_2Co_{1.5}Mn_{0.5}O_7$ oxide presents an excellent compatibility with CGO; in the PXRD pattern of a composite (70:30 wt %) heated at 900 ºC for 12 hours (not shown) only the Bragg

maxima due to these components are observed, discarding any reaction or decomposition and suggesting good long-term stability of these cathodes.

Polarization tests on symmetrical cells

Figure 7a shows the impedance spectrum of a $SrEu_2Co_{1.5}Mn_{0.5}O_7$/CGO/$SrEu_2Co_{1.5}Mn_{0.5}O_7$ symmetrical cell measured in air at 700 ºC. To separate the different contributions of the electrochemical process, the spectra have been fitted to a series circuit based on an inductance (L) caused by the wires of the electrochemical cell and equipment, an ohmic resistance (Rs) mainly associated to the total ion transport in the electrolyte and two parallel RQ-elements associated to processes at the electrolyte-electrode interface (oxide-ion transport) and at the electrode surface (oxygen reduction and ion transport), which take place at intermediate and low frequencies respectively.[25]

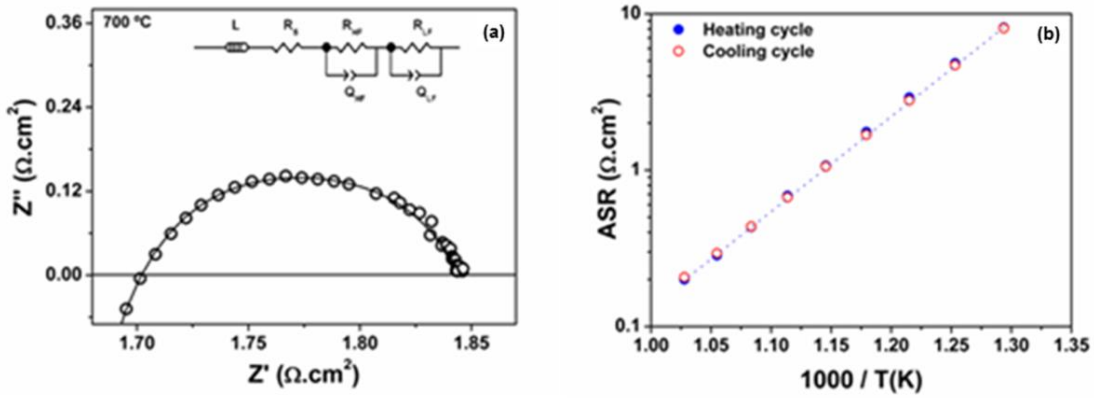

Figure 7. (a) Impedance spectrum for ESCM/CGO symmetrical cell at 700 ºC in air. The insets show the equivalent circuit used to fit the spectra. The solid line is the calculated spectrum using the equivalent circuit. **(b)** Arrhenius plot of the area-specific resistance (ASR) values.

The temperature dependence, in the range 550–700 ºC, of the ASR values (sum of resistances associated to processes at the electrolyte-electrode interface and on the electrode surface) determined from the impedance spectra is shown in Figure 7b. Similar values are obtained on both heating and cooling cycles, in agreement with the excellent chemical stability determined by TGA. These ASR values are the lowest reported for a R-P oxide. In this sense,0.15 Ω cm^2 is obtained at 700 ºC and similar values are only obtained at 800 ºC for $La_4Ni_{2.6}Co_{0.4}O_{10+\delta}$[12] and $NdSrCoO_{4+\delta}$[16], which is a significant higher temperature. Although lower ASR values are observed in $GdBaCo_2O_{6-\delta}$[43], this perovskite suffers important variations of the oxygen content with the temperature and shows a high TEC. In this connection, although the title compound does not loss oxygen on heating in air up to 900 ºC, the linear thermal expansion coefficient is anisotropic (α_a = 8.2(6) 10^{-6} K^{-1}, α_c = 40.1(4) 10^{-6} K^{-1}) and somewhat high along the c-axis which is the direction of the stacking of perovskite-like layers. The catalytic performance of the material for the oxygen reduction, characteristic of mixed conductors, may associated to the possible presence of interstitial oxygen atoms within the Eu-O planes.

A cross-sectional view of an electrode of composition $SrEu_2Co_{1.5}Mn_{0.5}O_7$/CGO (70:30 wt %) after operation is presented in Figure8. A good adherence between components is observed without any noticeable defects such as cracking or delamination in the interfaces. However large particles (of micron size) of the active material are covered by submicron particles of the electrolyte. For this reason, the microstructure of the cell-components should be further optimised for improving triple-boundary-interface and make the title compound a really competitive cathode material for IT-SOFCs.

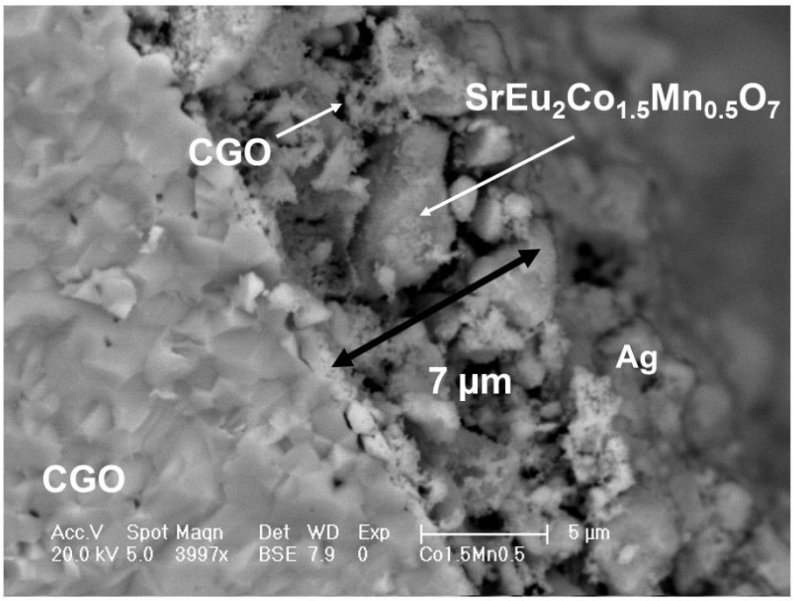

Figure 8. SEM micrograph of the (70:30wt %) cathode $SrEu_2Co_{1.5}Mn_{0.5}O_7$/CGO on CGO electrolyte.

Conclusions

The $SrEu_2Co_{1.5}Mn_{0.5}O_7$compound has been prepared and investigated as prospective cathode material for SOFCs. The crystal structure has been determined by X-ray diffraction and high-resolution electron microscopy. The Eu/Sr distribution over the two crystallographically distinct A-sites has been refined, which indicates complete cationic ordering. Tilting of the Co/MnO_6 polyhedra also occurs in the cubic-perovskite-like blocks. Such features have been confirmed by HAADF and ABF STEM study. The magnetic properties can be understood on the basis of the random distribution of Co^{3+} and Mn^{3+} ions and a short-range ordering of Co^{2+} and Mn^{4+} ions where the formation of ferromagnetic clusters (T_C= 121 K) takes place. Below 21 K a glassy magnetic behaviour is observed that may be explained taking into account intercluster interactions or the formation of a spin glass phase in the disordered

phase. From this Co/Mn atomic configuration a semiconductor-like behaviour can be inferred.

The thermal and chemical stability of the title compound have been also studied in order to perform electrochemical characterization as prospective cathode materials for IT-SOFCs. The impedance measurements on symmetrical cells using this material as electrode show the lowest ASR values reported so far for a R-P oxide (0.15 Ω cm^2at 700 ºC in air), proving important catalytic activity of the material for the oxygen reduction, characteristic of mixed conductors.

Author Information

Corresponding Author*

E-mail: khalid@ucm.es

Fax: (+) (34) 91 394 43 52

Author Contributions

Khalid Boulahya, Manar Hassan, Daniel Muñoz Gil, Julio Romero, Adrián Gómez Herrero, Susana García Martin, Ulises Amador. The manuscript was written through contributions of all authors. All authors have given approval to the final version of the manuscript. These authors contributed equally.

Acknowledgment

We thank the Ministerio de Economía y Competitividad (MINECO) and Comunidad de Madrid for funding the projects MAT2013-46452-C4-1-R and MAT2013-46452-C4-4-R, and S2013/MIT-2753, respectively.

References

1. A. N. Petrov, O. F. Kononchuk, A. V. Andreev, V. A. Cherepanov and P. Kofstad, *Solid State Ionics*, 1995, **80**, 189-199.
2. G. Briceno, H. Y. Chang, X. D. Sun, P. G. Schultz and X. D. Xiang, *Science*, 1995, **270**, 273-275.
3. A. C. Masset, C. Michel, A. Maignan, M. Hervieu, O. Toulemonde, F. Studer, B. Raveau and J. Hejtmanek, *Phys. Rev. B*, 2000, **62**, 166-175.
4. K. Boulahya, M. Parras and J. M. Gonzalez-Calbet, *Eur. J. Inorg. Chem.*, 2007, DOI: 10.1002/ejic.200700047, 2068-2071.
5. K. Boulahya, M. Parras and J. M. Gonzalez-Calbet, *Chem.-Eur. J.*, 2007, **13**, 910-915.
6. S. E. Dann, M. T. Weller and D. B. Currie, *J. Solid State Chem.*, 1991, **92**, 237-240.
7. S. N. Ruddlesden and P. Popper, *Acta Crystallographica*, 1957, **10**, 538-540.
8. S. N. Ruddlesden and P. Popper, *Acta Crystallographica*, 1958, **11**, 54-55.
9. L. Jantsky, H. Okamoto, M. Thomas, P. Karen, B. C. Hauback, M. J. Rosseinsky and H. Fjellvag, *Chem. Mat.*, 2014, **26**, 886-897.
10. F. Prado and A. Manthiram, *J. Solid State Chem.*, 2001, **158**, 307-314.
11. A. Aguadero, J. A. Alonso, M. J. Escudero and L. Daza, *Solid State Ionics*, 2008, **179**, 393-400.
12. G. Amow, J. Au and I. Davidson, *Solid State Ionics*, 2006, **177**, 1837-1841.
13. K. T. Lee, D. M. Bierschenk and A. Manthiram, *J. Electrochem. Soc.*, 2006, **153**, A1255-A1260.
14. K. T. Lee and A. Manthiram, *Chem. Mat.*, 2006, **18**, 1621-1626.
15. G. N. Mazo, S. M. Kazakov, L. M. Kolchina, A. V. Morozov, S. Y. Istomin, N. V. Lyskov, A. A. Gippius and E. V. Antipov, *J. Alloy. Compd.*, 2015, **639**, 381-386.
16. K. W. Song and K. T. Lee, *Ceram. Int.*, 2011, **37**, 573-577.
17. M. Al Daroukh, V. V. Vashook, H. Ullmann, F. Tietz and I. Arual Raj, *Solid State Ionics*, 2003, **158**, 141-150.
18. H. El Shinawi and C. Greaves, *J. Solid State Chem.*, 2008, **181**, 2705-2712.
19. C. Jin and J. Liu, *J. Alloy. Compd.*, 2009, **474**, 573-577.
20. S. J. Skinner and J. A. Kilner, *Solid State Ionics*, 2000, **135**, 709-712.
21. J. Rodríguez-Carvajal, *Physica B: Condensed Matter*, 1993, **192**, 55-69.
22. M. Yuste, J. C. Perez-Flores, J. R. de Paz, M. T. Azcondo, F. Garcia-Alvarado and U. Amador, *Dalton Trans.*, 2011, **40**, 7908-7915.
23. G. A. Bain and J. F. Berry, *J. Chem. Educ.*, 2008, **85**, 532-536.
24. D. Johnson, *ZView: A software Program for IES Analy*, 2005.
25. S. B. Adler, *Solid State Ionics*, 1998, **111**, 125-134.
26. S. B. Adler, *Chem. Rev.*, 2004, **104**, 4791-4843.

27. N. N. M. Gurusinghe, J. de la Figuera, J. F. Marco, M. F. Thomas, F. J. Berry and C. Greaves, *Mater. Res. Bull.*, 2013, **48**, 3537-3544.
28. A. V. Crewe, *Rep. Prog. Phys.*, 1980, **43**, 621-640.
29. S. D. Findlay, N. Shibata, H. Sawada, E. Okunishi, Y. Kondo and Y. Ikuhara, *Ultramicroscopy*, 2010, **110**, 903-923.
30. S. D. Findlay, N. Shibata, H. Sawada, E. Okunishi, Y. Kondo, T. Yamamoto and Y. Ikuhara, *Appl. Phys. Lett.*, 2009, **95**, 3.
31. S. J. Pennycook, Nellist, P.D. , *Scanning Transmission Electron Microscopy: Imaging and Analysis*, 2011, **Springer**.
32. R. Aso, D. Kan, Y. Shimakawa and H. Kurata, *Sci Rep*, 2013, **3**, 6.
33. P. D. Battle, M. A. Green, N. S. Laskey, J. E. Millburn, L. Murphy, M. J. Rosseinsky, S. P. Sullivan and J. F. Vente, *Chem. Mat.*, 1997, **9**, 552-559.
34. A. M. Glazer, *Acta Crystallogr. Sect. B-Struct. Commun.*, 1972, **B 28**, 3384-3392.
35. A. L. Chinelatto, K. Boulahya, D. Perez-Coll, U. Amador, C. Tabacaru, S. Nicholls, M. Hoelzel, D. C. Sinclair and G. C. Mather, *Dalton Trans.*, 2015, **44**, 7643-7653.
36. M. T. Azcondo, J. Romero de Paz, K. Boulahya, C. Ritter, F. Garcia-Alvarado and U. Amador, *Dalton Trans.*, 2015, **44**, 3801-3810.
37. K. V. Lamonova, E. S. Zhitlukhina, R. Y. Babkin, S. M. Orel, S. G. Ovchinnikov and Y. G. Pashkevich, *The Journal of Physical Chemistry A*, 2011, **115**, 13596-13604.
38. V. L. Joseph Joly, P. A. Joy and S. K. Date, *Solid State Communications*, 2002, **121**, 219-222.
39. T. Kyômen, R. Yamazaki and M. Itoh, *Chemistry of Materials*, 2003, **15**, 4798-4803.
40. T. Kyomen, R. Yamazaki and M. Itoh, *Chem. Mat.*, 2004, **16**, 179-184.
41. V. L. Joseph Joly, P. A. Joy and S. K. Date, *Materials Letters*, 2001, **51**, 172-176.
42. J. A. Mydosh, *Spin Glasses: An experimental Introduction*, Taylor and Francis, London, 1993.
43. D. Munoz-Gil, D. Perez-Coll, J. Pena-Martinez and S. Garcia-Martin, *J. Power Sources*, 2014, **263**, 90-97.